A full-field non-local crystal plasticity investigation of bi-layered HEA

Shuai Zhu, Emmanuel Brousseau *

Cardiff School of Engineering, Cardiff University, Cardiff CF24 3AA, United Kingdom

A B S T R A C T

Heterogeneous deformation has been widely proven to provide extra strengthening in heterostructured metallic materials. However, the explicit modelling of underlying plasticity mechanisms at both grain and sample levels remains a challenge for the scientific community. For this reason, the research presented here reports on the development and testing of a novel non-local crystal plasticity finite element model to simulate the deformation of heterostructured metallic materials. This model explicitly includes geometrically necessary dislocations (GNDs), back stress hardening, a damage criterion and does not rely on a homogenisation scheme. This approach enables the numerical investigation of dislocation-mediated plasticity simultaneously at both grain and sample levels. The model was validated against experimental data when simulating the deformation of a bi-layered high entropy alloy (HEA). The obtained results aligned well with experimental findings. In particular, the simulations confirmed that shear bands (SBs) preferably propagate along grains sharing similar orientation while causing severe grain rotation. In addition, for the pair of grain sizes considered here for the bi-layered HEA i.e., 14 μm and 46 μm for the finer and coarser layers, respectively, GNDs did not tend to pile up at the interface between these layers but at the grain boundaries instead. It is suggested that this study provides a solid theoretical framework for the future design of heterostructured metallic materials to achieve optimal strength-ductility balance and to predict potential crack nucleation sites and SB evolution in such materials.

1. Introduction

Metallic heterostructured materials consist of multiple zones of different metals or of various phases of the same constituent. These zones typically display different grain sizes and significant variation in their mechanical properties [1,2]. While conventional metallic materials can be engineered to exhibit some degree of heterogeneous microstructure, the distinguishing characteristic of heterostructured materials lies in the significant synergistic effect that results from the interactive coupling of their heterogeneous zones. Heterogeneous laminate, gradient, bi-modal grain size distribution and metal matrix composite structures are examples of such class of materials [2]. The mechanical properties of metal heterostructured materials largely exceed those predicted by the rule-of-mixtures of the properties of individual constitutive zones [2]. Under load, such materials also exhibit important hetero-deformation induced (HDI) synergistic strengthening [2]. Many studies have revealed that geometrically necessary dislocations (GNDs) are essential features of the micromechanics of heterostructured materials subjected to various loading conditions [3–5]. Heterostructures lead to strain partitioning between the harder and softer regions and in this case, an applied uniaxial strain is converted into multiaxial strains, activating multiple slip systems and encouraging dislocation hardening. SBs are also considered as an important feature of strain localisation in heterostructures [6–8]. The microstructure of such materials dominates the deformation mechanisms and the resulting macroscopic mechanical response [2]. For this reason, understanding the deformation mechanisms at play and their contribution on the microstructural level is key to correlating microstructure with mechanical properties. However, existing investigations towards this endeavour have been mostly experimental and primarily focussed on the processing and macroscopic mechanical behaviour of heterostructured materials [9]. Thus, it is argued that there is a need for complementary simulations and theoretical studies for the further understanding of underlying microscopic mechanisms with a view to identify the influence of separate hardening effects, as such phenomena are not easily accessible and observable separately through experimental methods.

To complement experimental research [10], numerical methods stand as a valuable tool for quantitatively establishing connections between microstructure and the macroscopic mechanical response of heterostructured materials, as well as for fine-tuning their

---

* Corresponding author.
E-mail address: BrousseauE@cardiff.ac.uk (E. Brousseau).

microstructural arrangement. Furthermore, the plastic deformation of heterostructured material contains complex interactions coupled across various length scales. This scale-coupling calls for multiscale frameworks to effectively investigate the mechanical behaviour of such materials. Therefore, the systematic investigation of dislocation behaviour within heterostructures is an important scientific endeavour, which entails conducting thorough numerical investigations coupling multiple mechanisms. Different numerical tools at various length scales have been adopted by the research community to attempt such studies on heterostructured materials, such as discrete dislocation dynamics (DDD) [11,12] and molecular dynamics (MD) [13]. However, conventional MD simulations encounter two major challenges when investigating dislocation behaviours. Firstly, the high strain rate nature of MD simulations often lacks relevance to the grain-level dislocation motion typical of heterostructured materials under quasi-static loading. Secondly, current studies have primarily focused on limited examples of dislocation motion due to computational costs. For example, the largest grain size adopted was 105 nm in [14], which is smaller than the range of grain size typically considered in heterostructured materials. Furthermore, in DDD simulation, plastic deformation is usually constrained to be smaller than 3 %, restricting the range of investigations on strain hardening behaviour under larger deformation [11]. Thus, while informative, these studies have limitations for providing a comprehensive understanding of dislocation behaviour on larger spatio-temporal scales. Simulating and understanding the contribution of individual mechanisms towards overall strain hardening requires a comprehensive numerical framework. Theoretical methods [15–18] and homogenised FEM modelling [19] have been used to generalise stress and strain relationships in samples with grain size gradient. In particular, the internal damage in a Cu-based heterostructured laminate was investigated in [20] using a homogenised modelling method. However, this study primarily focused on establishing correlations between sample-level mechanical responses and the microstructure without modelling grains explicitly. Although applying an homogenisation scheme is an efficient way to investigate the effects of multiple deformation mechanisms [21–24], it does not allow for a comprehensive understanding of the spatial distribution and evolution of deformation characteristics for each grain, and consequent effects on the local extra strength.

Despite extensive numerical work reported on the nanoscopic and macroscopic levels, the behaviour of grain-level interactions in heterostructured materials is comparatively less explored. The crystal plasticity finite element modelling (CPFEM) method typically serves as an advanced tool for investigating the impact of grain-level information on larger scales, while simultaneously capturing the spatio-temporal dynamics of dislocation-related deformation processes. Research efforts on investigating heterostructured materials via CPFEM can be classified into three categories. The first type is based on classical local CPFEM where the grain size effect is excluded. For example, CPFEM has been adopted for the investigation of cracks in gradient aluminium [25] and graphene/aluminium composites [26]. A local CPFEM was employed for the investigation of interfacial characteristics of metal matrix composites [27,28]. Although the classical CPFEM method allows for a direct grain-level determination of interactive mechanisms, the presence of significant dislocation hardening, and the resulting size effect, is neglected. During uniaxial tension, the non-uniform deformation-induced GNDs contribute to the strain hardening of heterostructured materials through forest hardening [29,30]. Thus, such classical crystal plasticity models are unlikely to be capable of capturing correctly deformations arising at grain boundaries [31]. The second type of CPFEM adopted for the investigation of heterostructured materials considers the grain size effect based on the Hall-Petch law [32–34] or experimentally defined functions [35]. A size-dependent crystal plasticity model containing dislocation slipping and deformation twinning was developed for the investigation of gradient nanostructured Twinning Induced Plasticity steels [36]. Damage evolution and mechanically driven grain growth during the deformation of gradient nano-grained materials were

also considered into the constitutive model to study the role of microstructure gradient in the overall plastic response [37]. CPFEM was also adopted to study the strengthening mechanisms of gradient medium entropy alloys [38]. Synergistic enhanced mechanical properties of gradient nanostructured metals were considered in [35] using size-dependent CPFEM where the dislocation density distribution relied on experimentally defined functions instead of a phenomenological Hall-Petch relation. This second type of CPFEM models typically introduces grain size dependent equations, which usually rely on extensive experiments and the calibration of required parameters. In comparison, the third type of CPFEM models naturally captures the extra hardening due to inhomogeneous plasticity. Such models physically describe the collective behaviour of dislocations associated with crystallographic relationships between adjacent grains. This modelling approach provides more physical meaning and represents an ideal tool for revealing the deformation mechanisms of metallic materials rather than mimicking stress-strain relations [5]. Such a non-local CPFEM approach coupled with GNDs and related kinematic hardening in gradient grained materials was developed in [5]. However, grains were not spatially resolved in this work as the authors used a homogenisation scheme when modelling the whole specimen. Such homogenisation scheme can describe the deformation heterogeneity between grains but it neglects such heterogeneity inside grains [39]. Mutual interactions of slip localisation processes at variable distances within the same grain or in neighbouring grains can affect grain deformation [40]. Thus, the effect of microstructural variations in heterostructured materials on the incipient plasticity and dislocation mechanisms remains largely unexplored. The explicit modelling of heterogeneous grained metals in large-scale polycrystal simulations can help accelerate microstructural design for improved strength and ductility. Of the many polycrystalline deformation modelling tools, the ones that should best meet the above challenges combine CPFEM and a full-field mechanical approach [40]. Nevertheless, recognising the significance of strengthening mechanisms and damage initiation is vital in constructing a comprehensive understanding of strengthening in metallic heterostructured materials. In a recent study, full field CPFEM has been adopted for the investigation of the low-cycle fatigue property of IN718 [41]. However, this was achieved in the context of a homogeneous-grained material and thus, not in the context of heterostructured materials.

In summary, while a non-local CPFEM model was developed for the investigation of heterostructured materials in [5,42], grains were not explicitly considered in these studies. As a result, mechanisms such as SB and grain rotation could not be captured. In light of this knowledge gap, a non-local full-field CPFEM model, which explicitly accounts for the interaction between dislocations and grain boundaries, is developed in this work. The non-local characteristic of the developed model is achieved by explicitly calculating GNDs at each integration point to account for the spatial re-distribution of dislocations due to their motions. The Johnson-Cook (JC) damage criterion is also adopted as a potential indicator for predicting microcrack nucleation. The non-local full-field nature of the model on the slip system level enables the direct investigation of strain gradient effects caused by internal deformation heterogeneities. Besides, given that an element represents a part of a grain in the established model, deformation heterogeneity can be considered both across grain boundaries and inside grains.

The outcome of the developed model was validated using experimental data from the literature. In particular, the study from Fu and co-workers [4], who fabricated bi-layered high entropy alloy (HEA) specimens utilising laser shock peening, was adopted as the benchmark against which the results of the developed model could be compared. This paper is organised as follows. In Section 2, the proposed non-local CPFEM modelling framework is introduced. In Section 3, uniaxial tensile simulations on homogenous grained HEAs with different grain sizes are conducted to validate the model. In Section 4, the proposed framework is applied to simulate the uniaxial tensile behaviour of a heterostructured HEA and the obtained results are compared with the

experimental data given in [4]. In addition, the deformation characteristics and strengthening mechanism of heterostructured materials are comprehensively discussed. Lastly, the conclusions of the research findings are presented in Section 5.

2. Numerical framework and FEM model

In this section, the development and implementation of a non-local CPFEM framework are presented. The framework incorporates essential components, including the slip model, the hardening model, and the calculation of GNDs, which contribute to the resultant back stress. Additionally, the implementation details of the model are discussed, providing a foundation for its application in simulating material behaviour at the microscale.

2.1. CPFEM constitutive model

2.1.1. Slip model

The shear strain rate $\dot{\gamma}^a$ generated by the dislocation motion of slip system a is expressed as [43]:

$$\dot{\gamma}^a = \dot{\gamma}_0 \left(\frac{|\tau^a|}{\tau_c^a} \right)^n sgn(\tau^a), \tag{1}$$

where $\dot{\gamma}_0$ is the reference shear rate, n is the power law exponent, τ^a is the shear stress acting on the slip system and τ_c^a is the critical resolved shear stress (CRSS) which describes resistance to gliding dislocations. The CRSS can be further formulated as [44]:

$$\tau_c^a = \left(\tau_c^a \right)^0 + \tau_{for}^a + \tau_{sub}^a, \tag{2}$$

where $\left(\tau_c^a \right)^0$ is the initial CRSS, τ_{for}^a is the forest dislocation interaction stress and τ_{sub}^a is the dislocation substructure interaction stress.

2.1.2. Hardening model

It was pointed out in [45] that meaningful boundary conditions for the dislocation evolution equations are required if they are to be applied to problems with more complex interfaces or open boundaries. Considering difference in properties between finer and coarser grain regions, the Kocks-Mecking-Estrin (KME) dislocation density model was adopted to account for dislocations generation and annihilation. Thus, the evolution of forest density for slip system a, $\Delta\rho_{for}^a$, is as follows [46]:

$$\Delta\rho_{for}^a = \left(k_1 \sqrt{\rho_{for}^a} - k_2(\dot{\varepsilon}, T)\rho_{for}^a \right) |\dot{\gamma}^a|\Delta t, \tag{3}$$

where k_1 is the hardening constant, Δt is the step time increment and k_2 is the annihilation constant. $k_1\sqrt{\rho_{for}^a}$ represents the rate of dislocation storage by statistical trapping of gliding dislocations by forest obstacles. $k_2(\dot{\varepsilon}, T)\rho_{for}^a$ accounts for dynamic recovery by thermally activated mechanisms such as dislocation cross-slip and climb, which can be obtained through [44]:

$$k_2 = k_1 \frac{\zeta b^a}{g^a} \left(1 - \frac{K_B T}{D^a (b^a)^3} \ln \frac{\dot{\varepsilon}}{\dot{\varepsilon}_0} \right), \tag{4}$$

where g^a is the effective activation enthalpy, D^a is the drag stress, $\dot{\varepsilon}_0$ reference slip rate.

The readers should note that while the first term of Eq. (3) primarily governs the evolution of mobile dislocation densities, the interaction with forest dislocations is accounted for through the hardening term, which reflects the strength of forest interactions. This is a common simplification in crystal plasticity models [46,51], as incorporating all dislocation types explicitly would significantly increase computational complexity without necessarily improving predictive accuracy. Besides, while the explicit modelling of dislocation types and the effect of grain

boundaries are beyond the scope of our current study, their effects are effectively captured by the phenomenological parameters that represent dislocation multiplication and annihilation. This simplification aligns with the intent of mesoscale models like that developed in this study, where the focus is on capturing aggregate behaviour rather than resolving individual dislocation mechanisms.

The hardening caused by forest dislocations τ_{for}^a can be expressed as:

$$\tau_{for}^a = \zeta G^a b^a \sqrt{\rho_{for}^a}, \tag{5}$$

where ζ is the dislocation interaction parameter, G^a is the shear modulus and b^a is the magnitude of the Burgers vector. Dynamic recovery is often associated with thermal activation of dislocation cross-slip and climb, and the formation of dislocation substructures is concomitant with these recovery processes. The term substructure dislocation is used to describe dislocations that are statistically stored within the substructure due to deformation and contribute to the total dislocation density. Substructure dislocations primarily arise from local plastic deformation processes and are essential for capturing the hardening behaviour. As a consequence, the rate of substructure dislocation $\Delta\rho_{sub}$ development was coupled to the rate of recovery of all active dislocations through [44]:

$$\Delta\rho_{sub} = q \sum_a f^a \sqrt{\rho_{sub}} k_2 \rho_{for}^a |\dot{\gamma}^a|\Delta t, \tag{6}$$

where q is the rate coefficient, f^a is the fraction of recovery rate that leads to substructure formation. Dislocation dynamics simulations show that the contribution to hardening by dislocations stored within substructures, such as cell walls, can be written with the following extended Taylor law [44]:

$$\tau_{sub} = k_{sub} G^a b^a \sqrt{\rho_{sub}} \ln \left(\frac{1}{b^a \sqrt{\rho_{sub}}} \right), \tag{7}$$

where k_{sub} is an empirical parameter.

2.2. GND calculation

The GND density is calculated from Nye's dislocation density tensor Λ [47], which can be expressed based on the curl of plastic deformation gradient $\mathbf{F}^p$ [48–50]:

$$\Lambda = \left(\nabla \times \mathbf{F}^{p^T} \right)^T. \tag{8}$$

Thus, the GND density ρ_{GND} can be obtained as:

$$\rho_{GND} = [A]^T \left([A][A]^T \right)^{-1} \{ \Lambda \}, \tag{9}$$

where $[A]$ is the linear operator matrix calculated based on slip line direction $\mathbf{t}$, slip plane normal $\mathbf{n}$ and Burgers vector $\mathbf{b}$. $\{ \Lambda \}$ is the vector form of the Nye's dislocation density tensor Λ. The GND density is calculated using singular value decomposition, followed by inversion to determine the dislocation densities. The solution is constrained to the active slip systems [51], which are identified based on the total slip magnitude of each slip system.

Via incorporating the effect of GNDs, the forest dislocation density ρ_{for}^a in Eq. (3) can be further modified by the projection of GNDs:

$$\rho_{for}^a = \Delta\rho_{for}^a + \sum_b \left| \mathbf{n}^a \cdot \mathbf{t}_e^b \right| \left| \rho_{GND,e}^b \right| + \left| \mathbf{n}^a \cdot \mathbf{s}_s^b \right| \left| \rho_{GND,s}^b \right|, \tag{10}$$

where $\mathbf{t}^b$ is the dislocation line direction, $\mathbf{n}^a$ is the slip plane normal, $\mathbf{s}^b$ is the slip direction. The calculation of hardening caused by forest dislocation τ_{for}^a in Eq. (5) and substructure dislocations $\Delta\rho_{sub}$ in Eq. (6) are updated accordingly. ρ_{tot}^a can be obtained as:

$$\rho_{tot}^a = \rho_{sub} + \sqrt{ \left(\rho_{GND,e}^a \right)^2 + \left(\rho_{GND,s}^a \right)^2 }. \tag{11}$$

A more detailed introduction regarding the fundamental aspects of the developed numerical framework including the definition of grain rotation can be found in [51,52].

2.3. Back stress model

Physically, the back stress results from the spatially heterogeneous distribution of GNDs [5,53]. High energy X-ray diffraction microscopy techniques proved that even at lower length-scale, the GND back stress model is in close agreement with the thermodynamic origin of back stress in a pure continuum mechanics framework of crystal plasticity constitutive relations [54]. Besides, it involves only one unknown parameter and enables one to initialise back stress at each point within a microstructure in the crystal plasticity analysis [54]. This is favourable considering the significant amount of initial dislocations induced by laser shock peening in the experimental work from Fu et al. [4], which is considered here for evaluating the outcomes of the model. In the context of this work, where the focus is on developing a full-field non-local crystal plasticity finite element model to investigate cooperative strengthening mechanisms in metallic heterostructured materials, it is of interest to probe the effect of GND-induced kinematic hardening on the strain hardening behaviour. Thus, following the work in [55], the back stress χ^a caused by GND density on slip system ρ^a_{GND} was calculated as:

$$\chi^a = KG^a b^a \sqrt{\rho^a_{GND}}, \tag{12}$$

where, K is a scaling constant. the shear modulus G^a used for each slip system is the macroscopic shear modulus of the material, which is assumed to be the same for all slip systems. It is noted that the back stress in Eq. (12) is formulated based on the magnitude of stress and does not explicitly consider its sign. This approach aligns with the assumption that the kinematic hardening evolution is driven by the absolute value of plastic deformation rather than the direction of the stress tensor components. This simplification is consistent with similar models in the literature [55].

Eq. (1) was further modified as:

$$\dot{\gamma}^a = \dot{\gamma}_0 \left(\frac{|\tau^a - \chi^a|}{\tau^a_c} \right)^n sgn(\tau^a - \chi^a). \tag{13}$$

Thus, this model connects the mathematical description of kinematic hardening, in the context of crystal plasticity, to the underlying mechanisms at the microscopic level.

2.4. Damage model

Stress mismatch between two regions results in high triaxiality [56,57], which is a key damage characteristic [58]. Thus, a reasonable damage model should be developed to investigate damage nucleation in heterostructured materials. Herein, the JC dynamic failure model, proven to be robust for microscale processes affected by large deformations [59,60], especially within a CPFEM framework [61], was adopted as the damage criterion. The JC failure model comprehensively includes the effect of strain hardening, strain rate and temperature. More specifically, the JC failure model is based on the calculation of the equivalent plastic strain, which is expressed as follows:

$$\bar{\varepsilon}^{pl}_f = (d_1 + d_2 e^{d_3\gamma}) \left(1 + d_4 \ln\left(\frac{\dot{\bar{\varepsilon}}^{pl}}{\dot{\varepsilon}_0}\right)\right) \left(1 + d_5 \frac{T - T_r}{T_m - T_r}\right), \tag{14}$$

where d_1 to d_5 are material damage parameters, γ is the stress triaxiality ratio, $\dot{\bar{\varepsilon}}^{pl}$ is the equivalent plastic strain rate, $\dot{\varepsilon}_0$ is the equivalent reference strain rate, T is the current temperature, T_r is the reference temperature and T_m is the material melting temperature. A summation of incremental failure strain $\Delta\bar{\varepsilon}^{pl}_f$ was carried out over all increments for assessing the failure criterion, ω [62]:

$$\omega = \sum \left(\frac{\Delta\bar{\varepsilon}^{pl}_f}{\bar{\varepsilon}^{pl}_f}\right), \tag{15}$$

where $\bar{\varepsilon}^{pl}_f$ is equivalent plastic strain. Failure is reached when this failure criterion, ω, reaches a value equal to "1″.

2.5. Model implementation

The developed non-local CPFEM model was implemented into a user-defined material subroutine (UMAT) [31,63,64]. The tensile simulations were performed with the commercial FEM software ABAQUS. Table 1 shows the material properties adopted in this work. As mentioned earlier, the experimental data used in this research to validate the developed model were those reported by Fu and co-workers [4], who investigated the heterostructured $CrFeCoNiMn_{0.75}Cu_{0.25}$ high entropy alloy. The studied HEA has face centred cubic (FCC) crystal structure, and the dominant slip system is {111}<110>. As material properties for this specific alloy are not all available from the literature, care was taken to select values relevant for this HEA.

3. Uniaxial tensile response of homogeneous HEA specimens

Before investigating the deformation behaviour of the bi-layered HEA specimen considered in this work, the tensile response of each separate homogeneous polycrystalline regions was simulated first. In this section, simulations were carried out to validate the ability of the developed model to capture the GND-induced effect and corresponding mechanisms. In particular, five homogeneous-grained models with grain size ranging from 5 μm to 100 μm were considered.

3.1. CPFEM modelling

A 2D model was employed to ease the computational burden. In particular, representative volume elements (RVEs) consisting of 32 randomly oriented grains as displayed in Fig. 1(a), were employed for the homogeneous-grained material simulations. The initial flow stress of FCC polycrystals depends both on the grain size and the initial dislocation density [5] and samples with the same grain size and dislocation density distribution, but randomly generated grain orientation, exhibit varied mechanical properties. In order to avoid the influence of the

Table 1
Material properties.

Parameter	Symbol	Value
Elastic moduli [65]	$C11$	264.6 GPa
	$C12$	184.8 GPa
	$C44$	112.9 GPa
Magnitude of the Burgers vector [66]	b	0.252 nm
Power law exponent	n	10
Initial CRSS	τ^0_c	101.5 MPa
Reference slip rate	$\dot{\gamma}_0$	0.001
Hardening constant	k_1	1
Dislocation interaction parameter	ζ	0.9
Effective activation enthalpy [66]	g^a	3×10^{-4}
Drag stress [66]	D^a	500 MPa
Reference slip rate	$\dot{\varepsilon}_0$	1×10^7
Rate coefficient [44]	q	4
Fraction of recovery rate	f^a	20
Empirical parameter	k_{sub}	0.086
References strain rate (s^{-1})	$\dot{\varepsilon}_{ref}$	1
Initial GND	ρ_0	10^{13}
Scaling constant of back stress [55]	K	0.4
Johnson Cook damage parameters [62]	d_1	0.54
	d_2	4.89
	d_3	-3.03
	d_4	0.014
	d_5	1.12
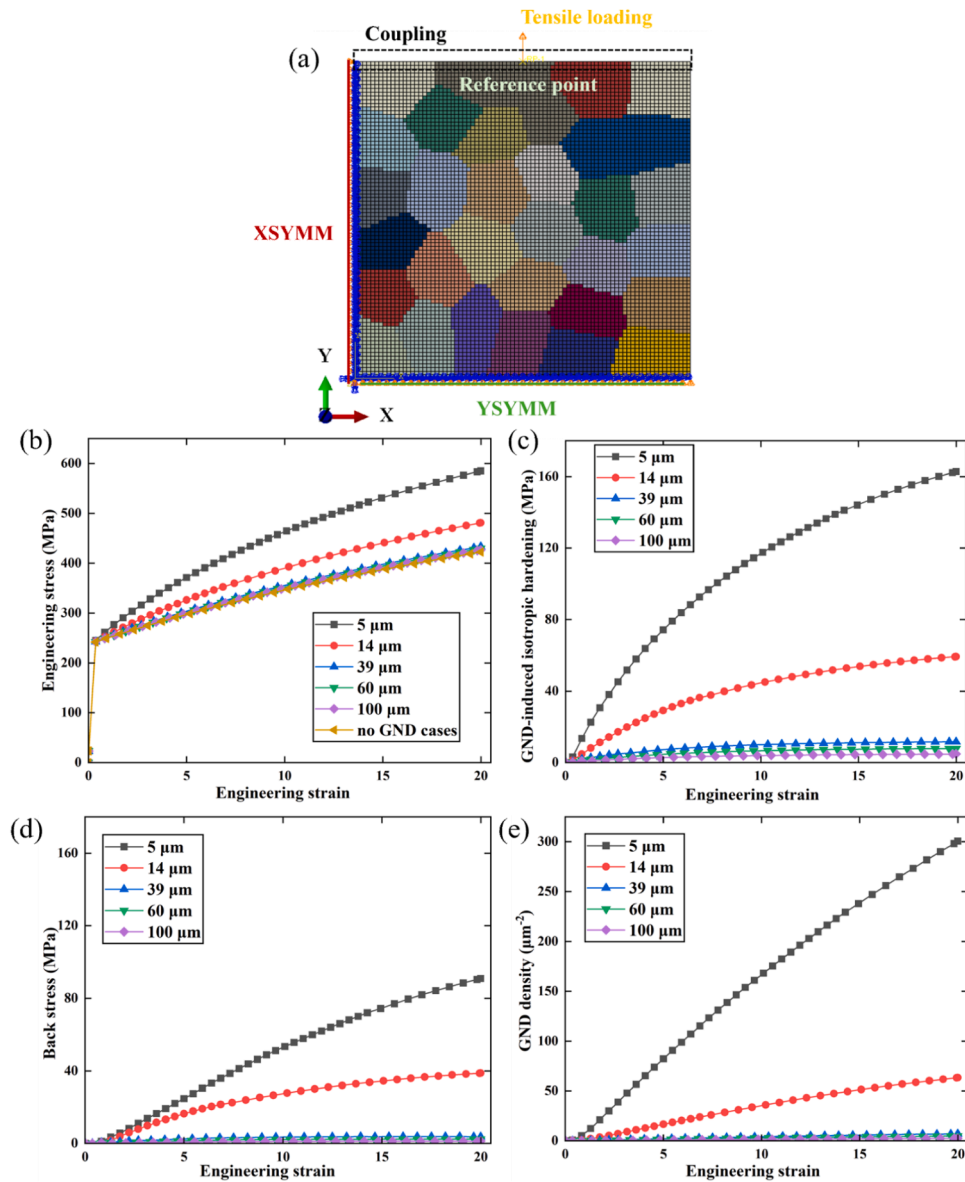
Fig. 1. (a) RVE containing 32 randomly orientated grains generated using the Voronoi algorithm and boundary conditions adopted during the finite element simulations. Simulated (b) stress-strain curves and (c) GND densities for homogeneous HEA polycrystals with grain sizes ranging from 5 μm to 100 μm. Results without GND hardening are also shown in (b) for comparison. Contribution of (d) back stress hardening and (e) GND-induced isotropic hardening to the flow stress for homogeneous HEA specimens with grain sizes in the range of 5 μm to 100 μm. These figures highlight a marked increase in strain hardening after the yield point with decreased grain size. The size effect is less significant when the grain size is above 60 μm.

initial dislocation density, it was set to 0.1/ μm^2 in all cases studied in this section. In addition, the grain orientation was kept constant between the different samples simulated here. The polycrystalline models with varying grain size were generated using the open-source software Neper [67]. They displayed the same grain morphology and were discretized using CPS4 elements. In other words, the parameters used for the validation work reported in this section, including grain orientations and initial dislocation density, were all identical apart from the grain size. In this way, the effect of the grain size could be isolated and effectively studied between the five homogeneous-grained models considered. An initial mesh sensitivity study showed that the mesh resolution adopted was sufficiently high for the modelled homogeneous polycrystals, as shown in the Appendix. To simulate uniaxial tensile deformation, displacement constraints of $U_x = 0$ and $U_y = 0$ were applied on the lower and left surfaces, respectively as displayed in Fig. 1 (a). Furthermore, for ease of data post-processing, a coupling constraint was applied to all the nodes on the top surface and the reference point to

ensure that their displacements and reaction forces along the y-axis were the same. The tensile displacement was applied at the reference point at a constant strain rate of 7.14 $\times$ 10^{-4} s^{-1}, aligned the experimental loading condition reported in [4] by Fu and co-workers. The material parameters adopted for this constitutive model were summarised earlier in Table 1.

3.2. Validation of the constitutive model and parameter calibration

Fig. 1(b) and (c) show the simulation results for the five homogeneous polycrystalline specimens with grains sizes ranging from 5 μm to 100 μm. Engineering stress-strain curves were computed from the force-displacement data obtained with the simulations. As shown in Fig. 1(b), all samples exhibit increasing flow stress with increasing strain, indicating strain hardening. It can also be observed that the flow stress increases gradually with the decrease of the grain size. Thus, it can be said that the developed model can predict the grain size effect without

introducing any grain size-dependent parameters in its set-up. When the grain size increases above 39 μm, the simulated stress-strain curves display minor variation, indicating that the grain size effect becomes rather weak. This is corroborated with the data given in Fig. 1(c) as the GND density tends to stabilise and be minimal at this grain size and higher. The stress-strain curves simulated without considering GND hardening were also obtained for all five specimens. However, these curves overlapped since the grain orientation was identical for all five cases simulated. For this reason, only one curve labelled "no GND cases" is displayed in Fig. 1(b) for comparison. From Fig. 1(b), it is also noted that the grain size does not contribute to the elastic limit, but only significantly affects the flow stress during the plastic deformation stage. Besides, while all simulated specimens show strain hardening, the strain hardening rate increases as the grain size decreases. This coincides with experimental results obtained from FCC metals [68] and the simulation data reported in [5,69]. The above results indicate that the developed model can be utilised to study grain size-dependent problems such as those for heterostructured materials.

3.3. Grain size effect

The back stress was calculated based on the simulated GND density following Eq. (12). To study their respective individual influence on the strain hardening behaviour, the GND-induced kinematic hardening i.e., the back stress, and the GND-induced isotropic hardening were separately assessed. Figs. 1(d) and 1(e) show the contribution of the back stress and of the GND-induced isotropic hardening on the flow stress, respectively. Fig. 1(d) indicates that the back stress emerges at the onset of plastic deformation. This agrees with the experimental findings from [29] and the numerical findings reported in [5] for gradient copper. The back stress keeps increasing during the whole deformation stage. This should result from the fact that physically, back stress is due to the spatially heterogeneous distribution of GNDs. In the initial deformation stage, back stress is linked to the piling up of GNDs at grain boundaries (GBs). During subsequent deformation, dislocation structures, such as cells and walls, also lead to heterogeneous distribution of dislocations, which further enhances back stress. As seen in Fig. 1(d), in the simulated
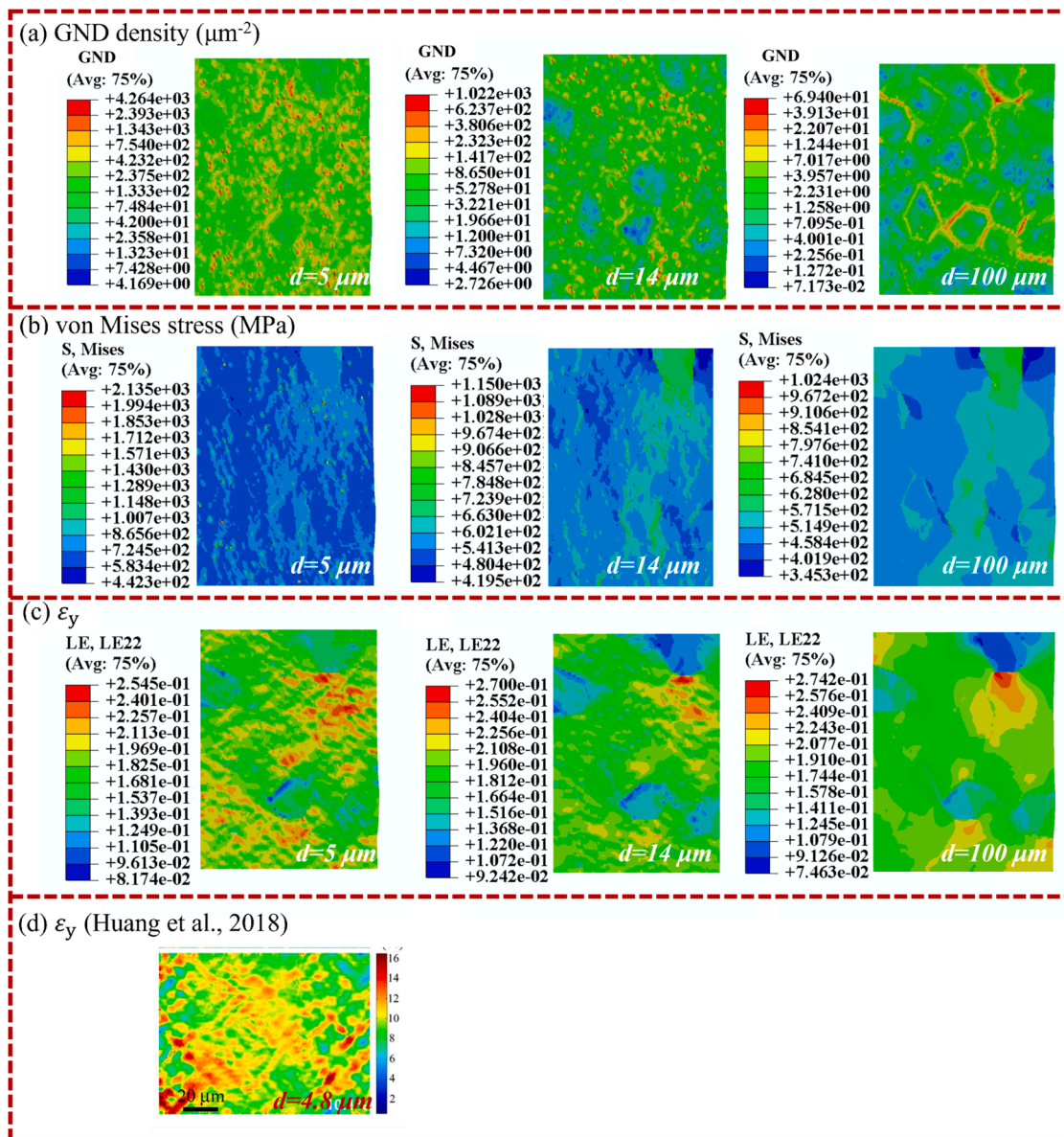

Fig. 2. Distribution of (a) the total GND density, (b) von Mises stress and (c) ε_y in the homogeneous grained HEA with grain size of 5 μm, 14 μm and 100 μm at a strain of 20 %, (d) example of experimental ε_y distribution on copper with a grain size of 4.8 μm obtained in [72] using Digital Image Correlation. ε_y represents the strain components in the loading direction. These figures highlight a marked increase in GND density, von Mises stress and ε_y with a reduction in grain size.

specimens with larger grain sizes, back stress hardly contributes to the flow stress, while it becomes more and more pronounced with decreasing grain size. This conclusion agrees with experimental results where metals with smaller grain sizes showed a stronger Bauschinger effect [5].

From Fig. 1(e), it can be seen that the GND-induced isotropic hardening increases with the strain. This agrees with the experimental results from [70] and the numerical predictions of [5,17]. It is also observed that GND-induced isotropic hardening is higher than the GND-induced kinematic hardening under the same applied strain for all grain sizes considered. Having said that, the plots shown in Fig. 1(d) and (e) suggest that when the grain size is larger than 39 μm, both GND-related effects can be neglected. Overall, based on these results, it can be inferred that the smaller the grain size, the stronger the GND-induced isotropic hardening and back stress. Besides, both GND-induced isotropic hardening and back stress emerge in a significant manner in the initial deformation stage for smaller grain size specimens and increase gradually afterwards.

To further understand the effect of GNDs on the deformation behaviour of the simulated polycrystals, Fig. 2(a) exhibits the evolution of the GND density across the modelled specimen, as well as the von Mises stress and ε_y for polycrystals with grain size of 5 μm, 14 μm and 100 μm. The GND density depicted here was calculated as:

$$\rho_{GND} = \sum_{\alpha=1}^{12} \left(|\rho_e^\alpha| + |\rho_s^\alpha| \right). \tag{16}$$

The above is a summation of absolute value of 12 edge dislocations, $\rho_{\Delta e}^\alpha$, and 6 screw dislocations, $\rho_{\Delta s}^\alpha$, on 12 slip systems. From Fig. 2(a), it is observed that the smaller the grain size, the more distributed the GND density is [45]. Moreover, the GNDs tend to accumulate near the GBs and especially at the triple junctions [71]. With the increase of grain size, the dislocation density decreases, and the magnitude of the difference in density between the GB regions and the grain interiors become smaller and smaller, indicating that the deformation in specimens with larger grain sizes is more homogeneous as evidenced by the von Mises stress distribution shown in Fig. 2(b). The strain along the tensile direction is displayed in Fig. 2(c). The deformation becomes more inhomogeneous with the appearance of dense SBs when the grain size decrease to 5 μm. The experimental strain distribution along the tensile loading direction on copper with a grain size of 4.8 μm obtained in [72] is also displayed in Fig. 2(d) for comparison. A good alignment is observed between the simulated results obtained here and those of [72] due to the grain size and FCC crystalline structure similarities.

In summary, based on the results presented in this section for homogeneous-grained specimens, it can be said that the simulations are reasonably consistent with experimentally-observed mechanical responses reported in the literature. Thus, the developed framework was further employed to investigate micromechanical mechanisms for heterostructured materials as these can be challenging to study experimentally. In next section, the local stress and strain distributions as well as the overall mechanical response are investigated in the case of the HEA heterostructured material from [4].

4. Uniaxial tensile response of a bi-layered HEA specimen

After the successful validation of the developed framework, in this section, the tensile deformation of a bi-layered HEA is simulated to investigate its strengthening mechanisms during deformation. Firstly, grain sizes of 14 μm, 39 μm and 60 μm were adopted to adhere to the grain size after LSP, recrystallization annealing (RA) and casting treatment, respectively, based on the work of Fu et al. [4]. Then, the strengthening mechanisms including SB formation and GND hardening of bi-layered HEA were investigated via the developed model.

4.1. Finite element model

The geometric model was divided into two regions, namely 1 and 2, as shown in Fig. 3(a), with each one characterised by a specific grain size according to the experimental data from Fu et al. [4]. In particular, region 1 had a grain size of 14 μm, while it was 46 μm for region 2. The interface between both regions was assumed to be perfectly bonded using plane strain condition. Following the LSP operations conducted in [4] by Fu and co-workers, the thickness of the surface and core layers was 300 μm and 700 μm, respectively. Accordingly, the thickness of the two regions in the model were set as 90 μm and 210 μm to keep the same ratio while reducing the computational burden. The overall size of the model was 300 μm along the x-axis and 600 μm along the y-axis. Uniaxial tension was applied in the y-direction at a strain rate of 7.14×10^{-4}/s on the reference point shown in Fig. 3(a). This reference point was also coupled with the top surface. The bottom surface was fixed on all degrees of freedom. Three paths of interest were selected as shown in Fig. 3(a) for plotting and investigating a number of state variables. As displayed in this figure, "Path A" traverses both regions in the middle of the specimen along its thickness. "Path B" corresponds to the interface between the two regions and "path C" cuts across the middle of region 1 in the direction of the y-axis, i.e. the loading direction.

4.2. Uniaxial tensile response

4.2.1. Stress-strain curves

Fig. 3(b) and (c) display the simulated stress-strain curves associated with different states of the HEA sample processed by Fu et al. [4]. More specifically, Fig. 3(b) displays results for cases where the specimen had a homogeneous grain size distribution, i.e. not in a bi-layered state. This corresponds to "as-cast" and the "recrystallization annealed" (RA) scenarios for which the grain size was 60 μm and 39 μm, respectively. The experimental tensile data obtained in [4] for these two cases are also displayed in Fig. 3(b) for comparison. Different from the previous section, where the dislocation density was intentionally set to 0.1/ μm^2 for all five models to isolate the effect of the grain size, the dislocation density in the as-cast and the RA model were set to 15/ μm^2 and 600/ μm^2 based on the report of [4], while the remaining parameters remained unchanged. Overall, the simulation results displayed in Fig. 3 (b) align with experimental data reasonably well for both cases. Slight deviations between the experimental and simulation results are observed mainly during the initial yielding stage. Thus, the reliability of the developed model is judged to be acceptable based on this comparison. In Fig. 3(c), the simulated and experimental engineering stress-strain characteristics of the bi-layered HEA are also compared. In this case, the experimental data considered from [4] are those following LSP. The simulated results for the stand-alone region 1 and for the standalone region 2 are also plotted for comparison. It can be seen from this figure that the simulated model with the finer grain size displays a higher flow stress and a flatter hardening curve, indicating limited strain hardening ability.

It should be noted that the values of the grain size considered here are fairly large, i.e. 14 μm and 46 μm for region 1 and 2, respectively. As reported in [73] and [32], a larger mechanical heterogeneity is beneficial for optimising the strength-ductility synergy. For this reason, it is expected that both GND-induced isotropic hardening and back stress hardening should have more significant effects on the strain hardening for samples combining nano-scale grains in the surface layer and micro-scale grain in their core [5].

4.2.2. Shear bands formation

In contrast with the homogenisation scheme used in [5,37] for the CPFEM simulation of gradient structures, one of the advantages of the full-field model developed here is that it enables the investigation of deformation morphology at grain level. This means that the distribution and evolution of local strain bands, also known as SBs [8,74] can be
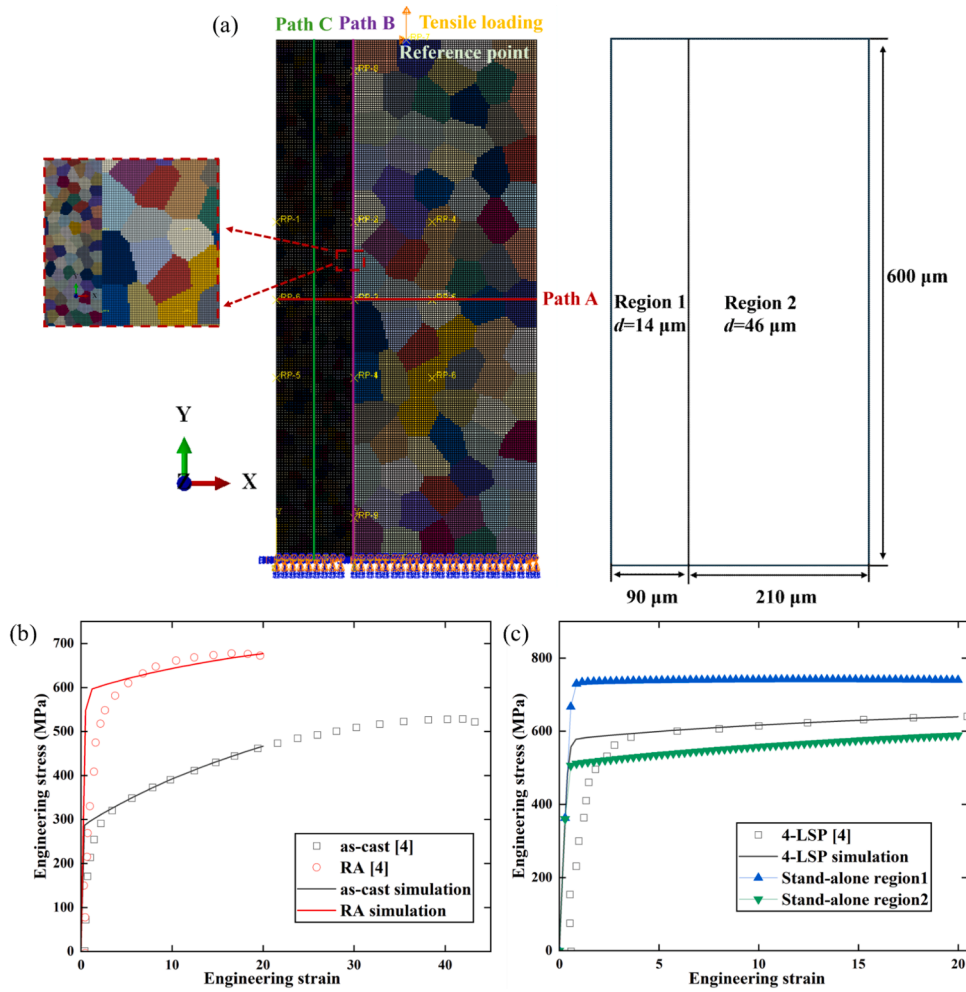
Fig. 3. (a) Finite element model of the bi-layered HEA specimen with different grain size, *d*, between both regions, geometric size, adopted constraint conditions and loading. Comparison of simulated and experimental engineering stress-strain curves for (b) as-cast and RA homogeneous HEA specimens; (c) bi-layered and stand-alone HEA regions 1 and 2. 4-LSP indicates four repetitions of the laser shock peening operation completed by the authors in [4]. The solid lines represent the simulation data, while the dots represent the experimental data. The strength of RA specimen is significantly higher than their as-cast counterparts, displaying efficient strengthening induced by finer grains.
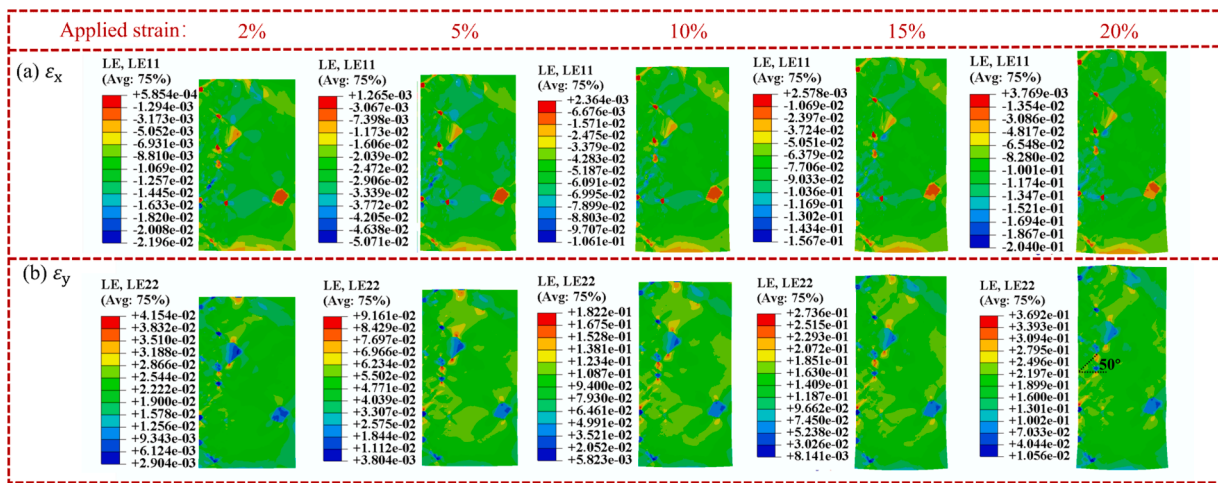

Fig. 4. Distributions of (a) ε_x and (b) ε_y in the simulated bi-layered HEA at strains of 2 %, 5 %, 10 %, 15 % and 20 %, with ε_x and ε_y referring to strain along *x* and *y* direction respectively. These figures highlight that SBs initiate at small strain in both regions and exhibit stable increase with elevated applied strain.

simulated. Fig. 4(a) and (b) show the local strain, ε_x, along the thickness and ε_y, in the tensile direction, respectively. It can be observed from these two figures that dense SBs are distributed over the sample during tensile deformation, and especially in region 1. These SBs tend to be orientated at about 50° with respect to the tensile axis (see Fig. 4(b)), which agrees with in-situ DIC analyses in [3,74–76]. Such dispersed SBs undertake large strain but none of them carries excessively high strain concentration, thus resulting in locally inhomogeneous, but globally uniform, strain distribution [3]. It is also observed from Fig. 4 that the SBs density decreases significantly in region 2. This implies that the low strain hardening capability of the harder layer, i.e., region 1, provides favourable conditions for the formation of SBs, as also evidenced in [3].

To further quantify the evolution of SBs under different tensile strains, the size and distribution of SBs along "Path A" and "Path C" (defined earlier with Fig. 3(a)) were statistically analysed as shown in Figs. 5. The larger peaks observed in these figures correspond to the location of SBs. From Figs. 5(a) and 5(c), which respectively display values for ε_x and ε_y along "Path C" (i.e., within region 1 and aligned with the tensile direction), it is seen that local strain intensities i.e., whether within SBs and in the surrounding matrix, increase with the applied strain. With further increase in applied strain, as displayed in Fig. 5(c) and Fig. 5(d), the increased amplitude in strain variation indicates that dense SB clusters are introduced by the extension and interaction of incipient SBs, which prevent the premature failure of heterostructured HEAs. While the width of SBs in the heterostructured HEA generally remains constant, their intensity increases linearly with the applied tensile strain as confirmed in Fig. 5(d). This result also aligns with the experimental finding from Fu and co-workers [4].

Figs. 5(b) and 5(d) show the distribution of SBs along "Path A", which crosses both regions through the middle of the specimen. During initial loading i.e., for a strain of 2 %, the values for ε_x and ε_y in region 2 remain relatively constant along this path, while these fluctuate in region 1. This indicates that SB nucleation originates in region 1, with the smaller grain size, and then propagate along the shear direction (see Fig. 5(d)). With increasing applied tensile strain, SBs also form in region 2 but with a lower density and magnitude. The local strain along both directions in region 1 is more heterogeneous than that in region 2 during loading, indicating a higher density of SBs. Subsequently, such strain gradient leads to differing plastic deformation behaviour between region 1 and region 2 during tensile loading. Based on Figs. 5 (b) and 5(d), it is noted that, while the respective magnitudes of ε_x and ε_y across both regions are generally comparable regardless of the applied strain, it is interesting to see that these strain values in region 2 tend to increase more steadily and smoothly. This suggests that the plastic deformation capacity in this softer region is higher than that in the harder region 1, which contains the smaller grains. In other words, plastic deformation is mainly driven by the core region 2. This result is aligned with the experimental findings of Fu and co-workers in [4] and with the stress-strain results shown earlier with Fig. 3(c), where the modelled bi-layered HEA displayed a work hardening behaviour closer to that of the stand-alone region 2.

4.2.3. GND hardening

In this section, the distributions of several pre-set internal state variables, namely GND density, von Mises stress and back stress, are analysed to understand grain-scale and sample-scale deformation features of the modelled bi-layered HEA. For heterostructured materials, in addition to GNDs pile-up near the grain boundaries, i.e., grain-scale GNDs, non-uniform deformation can arise due to the strain partitioning between the coarse-grained and the fine-grained layers resulting in the formation of sample-level GNDs [18,77]. Fig. 6(a) provides the simulated GND density at a strain of 20 % along "Path A". The inset included in the figure also shows the distribution of GNDs over the entire bi-layered specimen at this strain rate. It is observed from this simulated
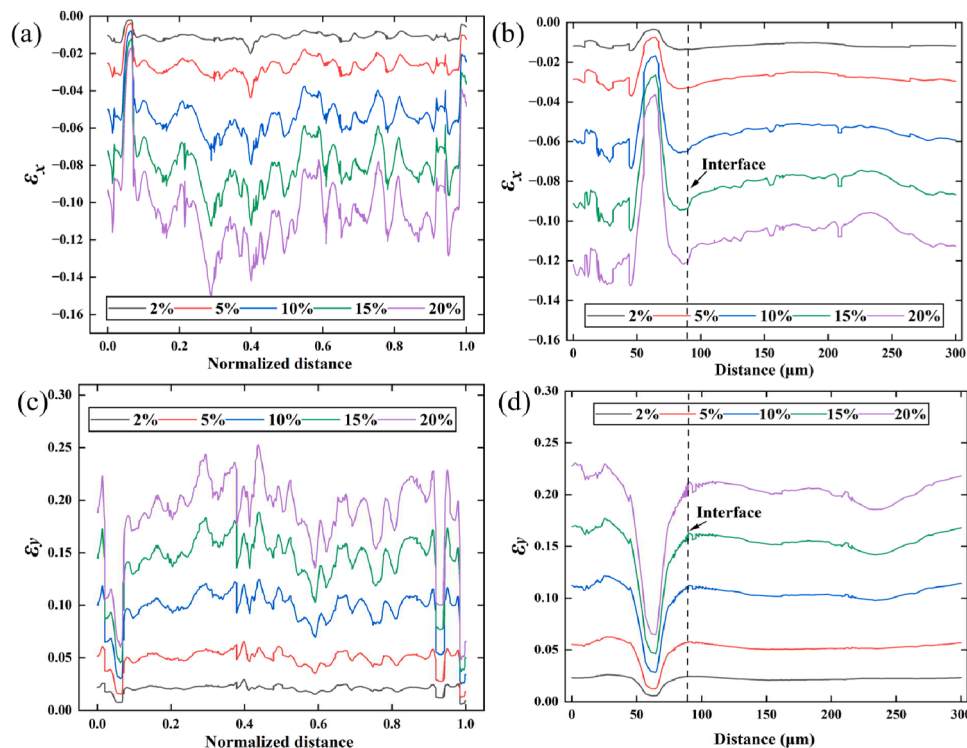

Fig. 5. Distributions of local strain ε_x (thickness direction) on (a) "Path C" i.e., within region 1 along the tensile direction, and (b) "Path A" i.e., along the thickness of the specimen across both regions, for the simulated bi-layered HEA at different tensile strains. Distributions of local strain ε_y (loading direction) on (c) "Path C" i.e., within region 1 along the tensile direction, and (d) "Path A" i.e., along the thickness of the specimen across both regions, for the simulated bi-layered HEA at different tensile strains. SBs initiate at small strain; the width of SBs in the modelled bi-layered HEA generally remains constant while their intensity increases linearly with the applied tensile strain.
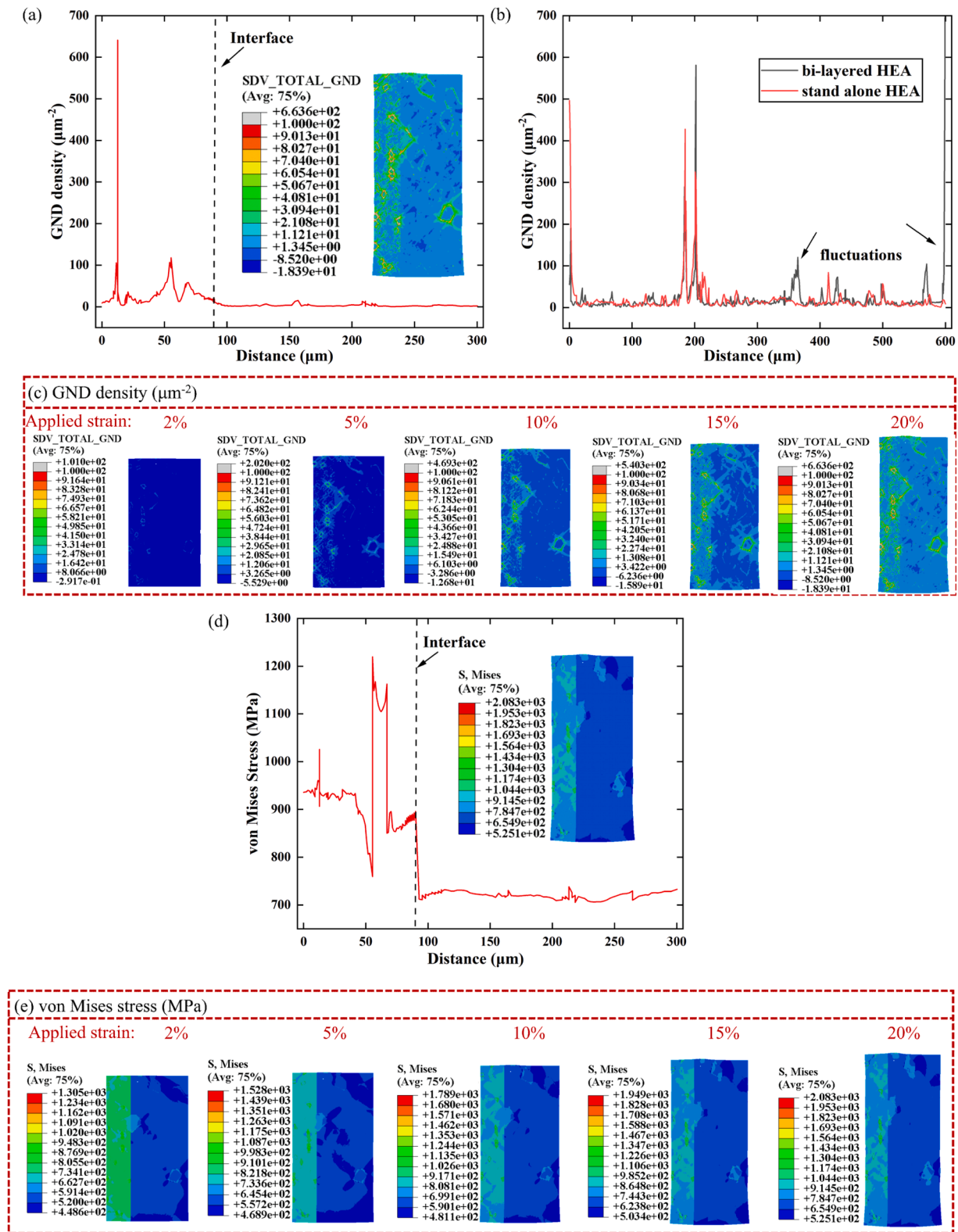
Fig. 6. GND density in the modelled bi-layered HEA at a strain of 20 % along (a) "Path A", and (b) "Path B". The red solid line and black solid line in (b) represent the stand-alone and bi-layered HEA, respectively. (c) Distributions of GNDs at strains of 2 %, 5 %, 10 %, 15 % and 20 %. Simulated (d) von Mises stress in the modelled bi-layered HEA along "Path A" for a strain of 20 % and (e) distributions of von Mises stress at strains of 2 %, 5 %, 10 %, 15 % and 20 % for the entire bi-layered HEA modelled. The GND density and von Mises stress are significantly higher and non-uniform in region 1 than that of region 2, displaying a stable increase with elevated applied strain.

data that the GND density is higher in region 1 and that dislocations accumulate preferentially at the grain boundaries. These findings also coincide with the experimental observation reported in [78] where GND density decreased from small grains to large grains in a CoCrFeNiMn gradient grained HEA. The higher dislocations density observed here in region 1 increases significantly with the applied strain during plastic deformation as shown in Fig. 6(c), which agrees with the experimental findings of [4]. From a qualitative viewpoint, Fig. 6(c) also suggests that a very small amount of GNDs formed at the interface between both regions. To gain further insights into the formation of such sample-level GNDs, Fig. 6(b) shows the simulated GND density at a strain of 20 % at the interface between regions 1 and 2 i.e., along "Path B". For comparison, the figure also includes the simulated GND density on the equivalent location on region 1 but when considered as a stand-alone region i.e., along its right edge when viewed from the top. Although slightly larger fluctuations of the GND density are observed in the bi-layered HEA compared to the stand-alone sample, it could be said that overall, the magnitude of GNDs at the interface for the bi-layered specimen is similar to that of the stand-alone model of region 1. This means that the formation of sample-level GNDs is not obvious for the bi-layered specimen modelled here. This is likely due to the fact that the difference in mechanical properties between both regions considered in this work is not significant as the difference in grain size between both is relatively small, i.e. a factor of 3.

Overall, the results given in Fig. 6(a-c) demonstrate that, for the pair of grain size values considered in the modelled bi-layered HEA i.e., 14 μm and 46 μm, there is no obvious concentrations of GNDs at the interface between regions 1 and 2. This observation is aligned with the results shown earlier with Figs. 5(b) and 5(d), which plotted the simulated strain at the interface. For the specific bi-layered HEA material modelled here, numerous grain-scale GNDs accumulate around GBs, especially in region 1, to accommodate the strain gradient between adjacent grains. Given that only a small amount of sample-level GNDs accumulate along the interface, it can be said that HDI strengthening originates largely from the accumulation of grain-scale GNDs in the case modelled here, rather than from sample-scale GNDs. This aligns with the experimental findings in [79] where the authors found that a only a small number of sample-scale GNDs accumulated around the interface between the coarse- and fine-grained regions of copper-brass laminates. Instead, the authors found that a large number of grain-scale GNDs accumulated around GBs to accommodate the strain gradient resulting from the heterogeneous deformation between neighbouring grains. The average grain size of the specimens considered by these authors in [79] was ~5.8 μm for the copper layers and ~1.1 μm for the brass layers. Thus, both grain sizes were on the microscale and there was a factor ~6 between them, which is somewhat comparable with the configuration of the specimen modelled here. It should be noted however, that the copper-brass laminates fabricated in [79] exhibited a ~7 μm gradient
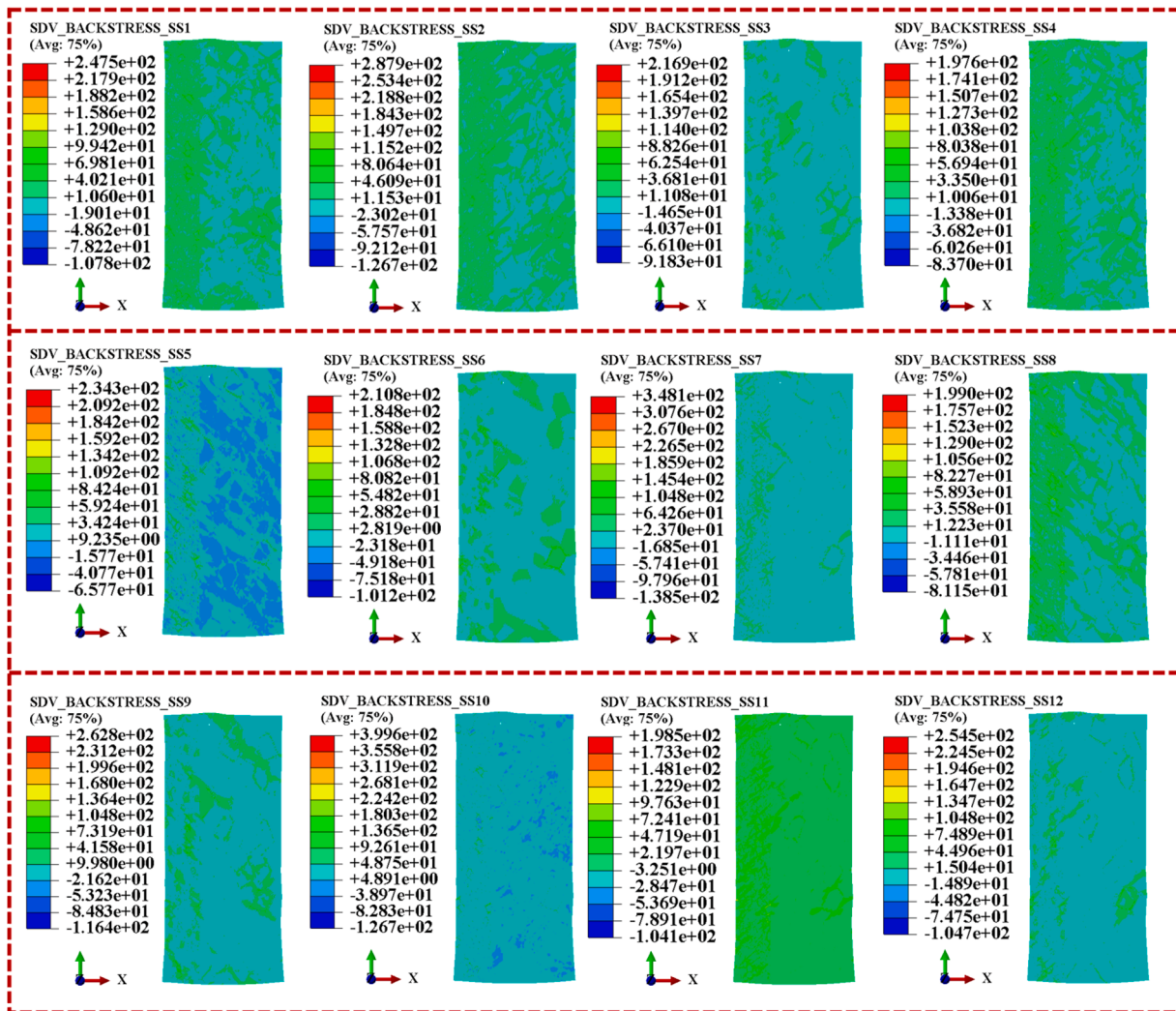

Fig. 7. Simulated distributions of back stress on the 12 slip systems in the modelled bi-layered HEA at a strain of 20 %. The back stress in region 1 is higher than that of region 2.

interface between the coarse- and fine-grained regions. This interface was composed of a gradient distribution of Zn and Cu elements. Such gradient interface, referred to as a "gradient transition layer" in [79] is not considered here. Indeed the interface between the HEA layers was modelled as a sharp transition in this work based on the experimental report in Fu et al. [4].

Fig. 6(d), which presents the distribution of the von Mises stress along "Path A" at a strain of 20 %, shows that the von Mises stress in region 1 is the highest. That is to say, region 1 carries more stress and region 2 experiences more plastic deformation. This agrees with the FEM simulations presented by Wang and co-workers in the case of polycrystalline metals with gradient grain sizes [34]. Furthermore, the stress along region 2 appears more homogeneous than that in region 1, where GNDs play a significant hardening role and no significant difference in stress values is noted between the grain interiors and the GBs in region 2.

Fig. 7 shows the distribution of back stress on the 12 slip systems at a strain of 20 %. Similar to the simulation data reported above for the von Mises stress and the GND density, qualitatively it is observed that the back stress increases with decreasing grain size. This is aligned with the stress-strain curves shown in Fig. 3(c) and with experimental measurements reported by [80,81], as well as with numerical predictions from [5]. This result also indicates that back stress originating from the smaller grains should be a non-negligible factor when considering back stress hardening in heterostructured materials.

4.2.4. Damage initiation

As presented earlier, the JC damage initiation criterion was also incorporated into the CPFEM framework. From Fig. 8(a), which presents
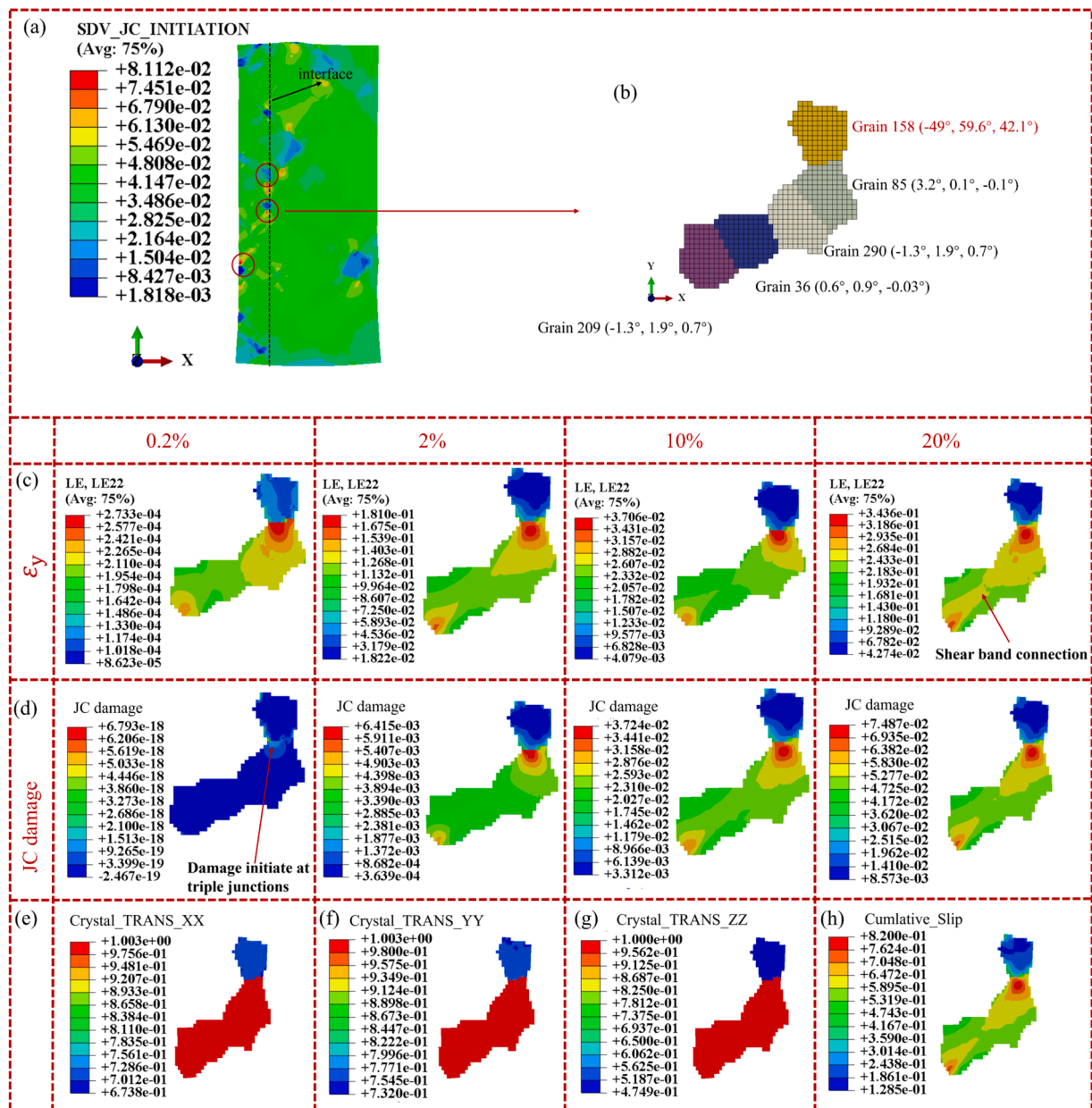

Fig. 8. (a) Distribution of JC damage factor values within the modelled bi-layered HEA for an applied strain of 20 %; (b) a locally enlarged region extracted from (a), composed of 5 grains with one of them displaying strong misalignment relative to the other four; evolution of (c) SBs and (d) damage within this extracted region for strain values between 0.2 % and 20 %; (e, f, g) crystal orientation within this region along the *x, y* and *z* direction, respectively, for an applied strain of 20 %, and (h) accumulated slip within this region, again for 20 % strain. LE22 represents the strain along loading direction. Red regions denote larger values, while blue regions represent smaller ones. These figures display that the SBs, JC damage, crystal rotation and slip accumulation tend to occur along grains sharing similar orientations.

the simulated damage criterion values for the whole bi-layered HEA specimen for an applied strain of 20 %, it can be seen that region 1 is relatively more prone to damage. This was reported at triple junctions formed by grains in [82,83]. SBs tend to form in alloys with fine grains due to their work hardening capability and eventually become crack initiation sites due to stress concentration [84,85]. Moreover, adjacent SBs can eventually connect with each other with the increase of tensile strain, as seen in Fig. 8(c) when the strain eventually reaches 20 %.

It was reported that SBs are likely to transmit into neighbouring grains with low GB misorientations [86]. MD simulations on a smaller grain size HEA also revealed that the rotation of grains can be triggered by grain boundary sliding and grain boundary migration as dominant mechanisms [71]. High intra- and inter-granular crystal rotation are plasticity mechanisms common to samples, which exhibit high mechanical performance [35]. Thus, the effect of grain orientation and rotation on the formation and propagation of SBs were also investigated in this work. In particular, the evolution of a typical SB spanning across 5 grains is analysed. This group of 5 grains is displayed in Fig. 8(b) including the respective Euler angles. Specifically, grains ID 85, 290, 36 and 209 exhibit similar orientations while the grain ID 158 has higher misorientation angles.

Figs. 8(c) and 8(d) present the SB and the JC damage factor evolution within this 5 grain region for strain values ranging from 0.2 % until 20 %. As seen in Fig. 8(c), the SB initiates at a triple junction for grains with significant different orientations. With the increase in strain, the SB then propagates within grains that share similar crystal orientations, i.e. grains ID 85, 290, 36 and 209. This simulation result agrees with experimental studies reported in [87] where microcracks occurred in both GBs and intra-grains under tensile conditions for a FCC metal with a homogenous composition of micro- and nano-scale grains. From Fig. 8 (d), it can be seen that there is a good alignment between the values of the JC damage criterion and the SB evolution. This suggests that the JC damage criterion could be employed as a suitable indicator to locate potential crack nucleation sites. For an applied strain of 20 %, Fig. 8 (e-g) shows that an appreciable amount of grain rotation took place for those grains traversed by the SB, in alignment with the experimental findings in [84]. In contrast, grain rotation is less severe for the grain ID 158, which had a higher initial misorientation compared to the other four grains. This observation is also in line with the experimental findings of [86] where the authors reported that the orientation of neighbouring grains affected the development of slip bands and their potential transmission. This is because the constraints placed on grains can be altered both by the grain size and the orientation-compatibility with neighbouring grains. Electron diffraction and imaging of the deformation sub-structures near SB interfaces reported in [88] also showed that an important part of the localization mechanism is non-uniform lattice re-orientations that cause a "geometrical softening" of the lattice. Thus, both the grain orientation distribution and the gradient distribution are deemed to be important structural features influencing the mechanical response [35]. Moreover, the accumulated slip in this 5 grain region is also displayed in Fig. 8(h) for an applied strain of 20 %. It is evident that the accumulated slip in the grain traversed by the SB is higher than that in the grain not affected by the SB.

5. Conclusions

The paper presented a novel non-local crystal plasticity model, which explicitly includes GNDs, back stress hardening and damage criterion. Importantly, the model does not employ a homogenisation scheme, which means that it can be employed to investigate dislocation-mediated plasticity at grain-level for heterostructured materials. The

model was implemented for a bi-layered HEA and its outcomes were validated against experimental data available from the literature. The model was able to confirm that the heterostructured HEA elicited heterogeneous deformation and consequent HDI strengthening during tension. Comparatively, low strain and high stress were observed in the region with smaller grains, while the coarser-grained region experienced lower stresses but more extensive plastic deformation. The more specific finding associated with this work are as follows:

The novel CPFEM framework developed here was able to reproduce and confirm a number of known experimental findings, namely that **a)** SBs and damage propagate among grains sharing similar orientation and **b)** significant rotation and slip take place in grains subjected to severe damage. Based on this, it is suggested that the properties of heterostructured materials could be further enhanced not only by controlling the grain size and dislocation density gradients, but also by controlling the initial grouping of grains and their respective orientations as well. Explicit modelling of orientation information of polycrystalline grains should be considered in future research. Indeed, a systematic study on the effect of grain orientation should pave the way towards a quantitative understanding of heterogeneous microstructures on the mechanical behaviour of a broader class of heterostructured materials. For the bi-layered HEA modelled here, GNDs accumulated at grain boundaries, rather than at the hetero-interface. Future work should investigate whether a threshold exists with respect to the size ratio between fine and coarse grain regions for which GNDs accumulation at interfaces becomes more prominent than grain-scale GNDs. It is suggested that the JC damage criterion could also be employed to characterise SBs evolution, which in turn could lead to the identification of potential crack nucleation sites.

It is worth noting that while this study focussed on a single phase bi-layered heterostructured HEA, the CPFEM framework developed here could also be applied to FCC/BCC alloys with different phases. It is also worth mentioning that the presented simulations were based on a 2D model with a focus on dislocation activities, and that this offers a computationally efficient approach compared to 3D cases with multiple mechanisms.

CRediT authorship contribution statement

Shuai Zhu: Writing – original draft, Visualization, Validation, Software, Methodology, Investigation, Conceptualization. **Emmanuel Brousseau:** Writing – review & editing, Supervision, Formal analysis.

Declaration of competing interest

The authors declare that they have no known competing financial interests or personal relationships that could have appeared to influence the work reported in this paper.

Acknowledgements

Appendix. : mesh convergence

To demonstrate that the mesh resolution is sufficiently high in this work, a 3D RVE with 10 grains is generated with different mesh numbers: 2304, 3600 and 4624, using Neper. The tensile stress-strain curves with different mesh resolutions are shown in Fig. A1 below. The results indicate that as the element number increases from 2304 to 4624, the stress-strain curves nearly overlap. Therefore, to ensure the accuracy of the results and reduce the computation cost simultaneously, 200 elements per grain are used for mesh in this work.
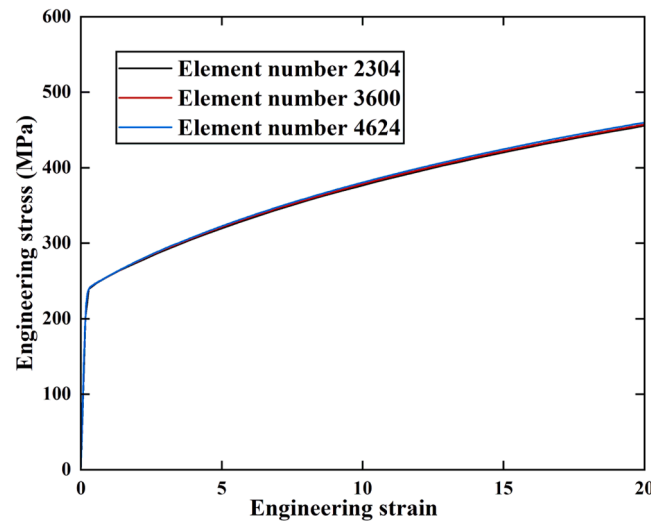

Fig. A1. Mesh convergence study on the developed framework.

Data availability

Data will be made available on request.

References

[1] Ji W, Zhou R, Vivegananthan P, Wu MSee, Gao H, Zhou K. Recent progress in gradient-structured metals and alloys. Prog. Mater. Sci. 2023;140:101194.
[2] Zhu Y, Wu X. Heterostructured materials. Prog. Mater, Sci. 2023;131:101019.
[3] Fu W, Sun Y, Fan G, Huang Y, Ning Z, Li X, Wang K, Sun J, Jiang S. Strain delocalization in a gradient-structured high entropy alloy under uniaxial tensile loading. Int. J. Plasticity 2023;171.
[4] Fu W, Huang Y, Sun J, Ngan AHW. Strengthening CrFeCoNiMn0.75Cu0.25 high entropy alloy via laser shock peening. Int. J. Plasticity 2022;154.
[5] Zhang X, Zhao J, Kang G, Zaiser M. Geometrically necessary dislocations and related kinematic hardening in gradient grained materials: A nonlocal crystal plasticity study. Int. J. Plasticity 2023;163:103553.
[6] Chen T, Li J. Modelling the shear banding in gradient nano-grained metals. NanoMater. 2021.
[7] Wang Y, Huang C, Li Z, Fang X, Wang M, He Q, Guo F, Zhu Y. Shear band stability and uniform elongation of gradient structured material: role of lateral constraint. Extreme Mech. Lett. 2020;37.
[8] Wang Y, Huang C, Li Y, Guo F, He Q, Wang M, Wu X, Scattergood RO, Zhu Y. Dense dispersed shear bands in gradient-structured Ni. Int. J. Plasticity 2020;124:186–98.
[9] Fu W, Li H, Huang Y, Ning Z, Sun J. A new strategy to overcome the strength-ductility trade off of high entropy alloy. Scripta Materialia 2022:214.
[10] Moering J, Ma X, Malkin J, Yang M, Zhu Y, Mathaudhu S. Synergetic strengthening far beyond rule of mixtures in gradient structured aluminum rod. Scripta Materialia 2016:122:106–9.
[11] Lu S, Zhao J, Huang M, Li Z, Kang G, Zhang X. Multiscale discrete dislocation dynamics study of gradient nano-grained materials. Int. J. Plasticity 2022;156: 103356.
[12] Lu S, Ao N, Kan Q, Wu S, Kang G, Zhang X. Effect of residual stress in gradient-grained metals: dislocation dynamics simulations. Int. J. Mech. Sci. 2023;256: 108518.
[13] Lu X, Ran H, Cheng Q, Guo F, Huang C. Underlying mechanisms of enhanced plasticity in Ti/Al laminates at elevated temperatures: A molecular dynamics study. J. Mater. Res. Technol. 2024;28:31–42.
[14] Li W, Yuan F, Wu X. Atomistic tensile deformation mechanisms of Fe with gradient nano-grained structure. AIP Adv. 2015;5.
[15] Li J, Chen S, Wu X, Soh AK. A physical model revealing strong strain hardening in nano-grained metals induced by grain size gradient structure. Mater. Sci. Eng. 2015;620:16–21.
[16] Li J, Lu W, Chen S, Liu C. Revealing extra strengthening and strain hardening in heterogeneous two-phase nanostructures. Int. J. Plasticity 2020;126:102626.

[17] Li J, Soh AK. Modeling of the plastic deformation of nanostructured materials with grain size gradient. Int. J. Plasticity 2012;39:88–102.
[18] Li J, Weng GJ, Chen S, Wu X. On strain hardening mechanism in gradient nanostructures. Int. J. Plasticity 2017;88:89–107.
[19] Guo Z, Zhou J, Sun Z, Retraint D, Panicaud B. Modelling mechanical behaviour of a gradient-microstructured material obtained by surface mechanical attrition treatment accounting for residual stresses. Mech. Mater. 2023;184.
[20] Zhu S, Brousseau E, Shao Y, Peng W. Numerical investigation of internal damage in heterogeneous-structured laminates using a 3D multiple physical mechanisms based constitutive model. Compos. Struct. 2024.
[21] Zhao J, Liu B, Wang Y, Liang Y, Li J, Zhang X. Dispersed strain bands promote the ductility of gradient nano-grained material: A strain gradient constitutive modeling considering damage effect. Mech. Mater. 2023;179:104599.
[22] Zhao J, Kan Q, Zhou L, Kang G, Fan H, Zhang X. Deformation mechanisms based constitutive modelling and strength-ductility mapping of gradient nano-grained materials. Mater. Sci. Eng. 2019;742:400–8.
[23] Zhao J, Lu X, Liu J, Bao C, Kang G, Zaiser M, Zhang X. The tension-compression behavior of gradient structured materials: A deformation-mechanism-based strain gradient plasticity model. Mech. Mater. 2021;159:103912.
[24] Zhao J, Lu X, Yuan F, Kan Q, Qu S, Kang G, Zhang X. Multiple mechanism based constitutive modeling of gradient nanograined material. Int. J. Plasticity 2020;125: 314–30.
[25] Liu L-Y, Yang Q-S, Liu X, Nian X-C. Crystal cracking of grain-gradient aluminum by a combined CPFEM-CZM method. Eng. Fract. Mech. 2021:242.
[26] Liu L-Y, Yang Q-S, Liu X, Shang J-J. Modeling damage evolution of graphene/aluminum composites considering crystal cracking and interface failure. Compos. Struct. 2021:267.
[27] Zhang YB, Song SJ, Liu F. Thermo-kinetic characteristics on stabilizing hetero-phase interface of metal matrix composites by crystal plasticity finite element method. J. Mater. Sci. Technol. 2024;169:53–67.
[28] Zhang YB, Song SJ, Liu F. Thermo-kinetic orientation study on interface behavior of polycrystalline Cu-Nb composite by crystal plasticity finite element method. Mater. Design 2022:223.
[29] Cheng Z, Zhou H, Lu Q, Gao H, Lu L. Extra strengthening and work hardening in gradient nanotwinned metals. Sci. 2018;362:eaau1925.
[30] Wu X, Jiang P, Chen L, Yuan F, Zhu YT. Extraordinary strain hardening by gradient structure. Proc. Natl. Acad. Sci. 2014;111:7197–201.
[31] Liang H, Dunne FPE. GND accumulation in bi-crystal deformation: crystal plasticity analysis and comparison with experiments. Int. J. Mech. Sci. 2009;51:326–33.
[32] Zhang Y, Chen H, Jia Y-F, Li D-F, Yuan G-J, Zhang X-C, Tu S-T. A modified kinematic hardening model considering hetero-deformation induced hardening for bimodal structure based on crystal plasticity. Int. J. Mech. Sci. 2021;191.
[33] Zeng Z, Li X, Xu D, Lu L, Gao H, Zhu T. Gradient plasticity in gradient nano-grained metals. Extr. Mech. Lett. 2016;8:213–9.
[34] Wang Y, Yang G, Wang W, Wang X, Li Q, Wei Y. Optimal stress and deformation partition in gradient materials for better strength and tensile ductility: A numerical investigation. Sci. Rep. 2017;7:10954.

[35] Griesbach C, Bronkhorst CA, Thevamaran R. Crystal plasticity simulations reveal cooperative plasticity mechanisms leading to enhanced strength and toughness in gradient nanostructured metals. Acta Materialia 2024;270.

[36] Lu X, Zhao J, Wang Z, Gan B, Zhao J, Kang G, Zhang X. Crystal plasticity finite element analysis of gradient nanostructured TWIP steel. Int. J. Plasticity 2020;130: 102703.

[37] Lu X, Zhang X, Shi M, Roters F, Kang G, Raabe D. Dislocation mechanism based size-dependent crystal plasticity modeling and simulation of gradient nano-grained copper. Int. J. Plasticity 2019;113:52–73.

[38] Zhang X, Gui Y, Lai M, Lu X, Gu J, Wang F, Yang T, Wang Z, Song M. Enhanced strength-ductility synergy of medium-entropy alloys via multiple level gradient structures. Int. J. Plasticity 2023;164.

[39] Wu Y, Shen Y, Chen K, Yu Y, He G, Wu P. Multi-scale crystal plasticity finite element method (CPFEM) simulations for shear band development in aluminum alloys. J. Alloys Compd. 2017;711:495–505.

[40] Stinville JC, Charpagne MA, Maaß R, Proudhon H, Ludwig W, Callahan PG, Wang F, Beyerlein IJ, Echlin MP, Pollock TM. Insights into plastic localization by crystallographic slip from emerging experimental and numerical approaches. Ann. Rev. Mater. Res. 2023;53:275–317.

[41] Xi N, Ni Z, Liu P, Zhou Y, Fang X, Chen Z, Huang K. Prediction of low-cycle fatigue properties of additive manufactured IN718 by crystal plasticity modelling incorporating effects from crystallographic orientations and defects. Virtual Phys. Prototyp. 2024;19.

[42] Zhang Y, He C-Y, Wang X, Hama T, Sun B, Jia Y-F, Zhang X-C, Tu S-T. Revealing the fatigue strengthening and damage mechanisms of surface-nanolaminated gradient structure. Int. J. Plasticity 2024;104128.

[43] Ashby MF. The deformation of plastically non-homogeneous materials. Philosoph. Mag. 1970;21:399–424.

[44] McCabe RJ, Capolungo L, Marshall PE, Cady CM, Tomé CN. Deformation of wrought uranium: experiments and modeling. Acta Materialia 2010;58:5447–59.

[45] Wulfinghoff S, Böhlke T. Gradient crystal plasticity including dislocation-based work-hardening and dislocation transport. Int. J. Plasticity 2015;69:152–69.

[46] Mecking H, Kocks UF. Kinetics of flow and strain-hardening. Acta Metallurgica 1981;29:1865–75.

[47] Nye JF. Some geometrical relations in dislocated crystals. Acta Metallurgica 1953; 1:153–62.

[48] Arsenlis A, Parks DM. Crystallographic aspects of geometrically-necessary and statistically-stored dislocation density. Acta Materialia 1999;47:1597–611.

[49] Demir E, Martinez-Pechero A, Hardie C, Tarleton E. Restraining geometrically-necessary dislocations to the active slip systems in a crystal plasticity-based finite element framework. Int. J. Plasticity 2024.

[50] Das S, Hofmann F, Tarleton E. Consistent determination of geometrically necessary dislocation density from simulations and experiments. Int. J. Plasticity 2018;109: 18–42.

[51] Demir E, Martinez-Pechero A, Hardie C, Tarleton E. OXFORD-UMAT: an efficient and versatile crystal plasticity framework. Int. J. Solids Struct. 2024.

[52] Beausir B, Tóth LS, Neale KW. Ideal orientations and persistence characteristics of hexagonal close packed crystals in simple shear. Acta Materialia 2007;55: 2695–705.

[53] Zhang Y, Cheng Z, Zhu T, Lu L. Mechanics of gradient nanostructured metals. J. Mech. Phys. Solids 2024.

[54] Bandyopadhyay R, Gustafson SE, Kapoor K, Naragani D, Pagan DC, Sangid MD. Comparative assessment of backstress models using high-energy X-ray diffraction microscopy experiments and crystal plasticity finite element simulations. Int. J. Plasticity 2021;136.

[55] Kapoor K, Yoo YSJ, Book TA, Kacher JP, Sangid MD. Incorporating grain-level residual stresses and validating a crystal plasticity model of a two-phase Ti-6Al-4 V alloy produced via additive manufacturing. J. Mech.Phys. Solids 2018;121:447–62.

[56] Yu WX, Liu BX, Cui XP, Dong YC, Zhang X, He JN, Chen CX, Yin FX. Revealing extraordinary strength and toughness of multilayer TWIP/Maraging steels. Mater. Sci. Eng. 2018;727:70–7.

[57] Liu BX, Huang LJ, Kaveendran B, Geng L, Cui XP, Wei SL, Yin FX. Tensile and bending behaviors and characteristics of laminated Ti-(TiBw/Ti) composites with different interface status. Compos. Part B. 2017;108:377–85.

[58] Tvergaard V, Huang Y, Hutchinson JW. Cavitation instabilities in a power hardening elastic-plastic solid. Department of Solid Mechanics, Technical University of Denmark; 1990.

[59] Wang Z, Zhang H, Li Z, Li G, Zhang J, Zhang J, Hassan Hu, Yan Y, Hartmaier A, Sun T. Crystal plasticity finite element simulation and experiment investigation of nanoscratching of single crystalline copper. Wear 2019;430-431:100–7.

[60] Lai X, Li H, Li C, Lin Z, Ni J. Modelling and analysis of micro scale milling considering size effect, micro cutter edge radius and minimum chip thickness. Int. J. Mach. Tools Manufact. 2008;48:1–14.

[61] Boubaker HB, Moufki A, Nouari M, Laheurte P, Tidu A. Thermodynamically consistent formulation coupling crystal plasticity theory and Johnson-Cook damage model to simulate micromachining of copper. Procedia CIRP 2021;102: 506–11.

[62] Johnson GR, Cook WH. Fracture characteristics of three metals subjected to various strains, strain rates, temperatures and pressures. Eng. Fract. Mech. 1985;21:31–48.

[63] Dunne FPE, Rugg D, Walker A. Lengthscale-dependent, elastically anisotropic, physically-based hcp crystal plasticity: application to cold-dwell fatigue in Ti alloys. Int. J. Plasticity 2007;23:1061–83.

[64] Hardie C, Long DJ, Demir E, Tarleton E, Dunne FPE. A robust and efficient hybrid solver for crystal plasticity. Int. J. Plasticity 2023;170.

[65] Fang Q, Chen Y, Li J, Jiang C, Liu B, Liu Y, Liaw PK. Probing the phase transformation and dislocation evolution in dual-phase high-entropy alloys. Int. J. Plasticity 2019;114:161–73.

[66] Gao TJ, Zhao D, Zhang TW, Jin T, Ma SG, Wang ZH. Strain-rate-sensitive mechanical response, twinning, and texture features of NiCoCrFe high-entropy alloy: experiments, multi-level crystal plasticity and artificial neural networks modeling. J. Alloys Comp. 2020;845.

[67] Quey R, Dawson PR, Barbe F. Large-scale 3D random polycrystals for the finite element method: generation, meshing and remeshing. Comput. Methods in Appl. Mech. Eng. 2011;200:1729–45.

[68] Fang TH, Li WL, Tao NR, Lu K. Revealing extraordinary intrinsic tensile plasticity in gradient nano-grained copper. Sci. 2011;331:1587–90.

[69] Haouala S, Lucarini S, Llorca J, Segurado J. Simulation of the Hall-Petch effect in FCC polycrystals by means of strain gradient crystal plasticity and FFT homogenization. J. Mech. Phys. Solids 2020;134:103755.

[70] Zhang S, Liu W, Wan J, Misra RDK, Wang Q, Wang C. The grain size and orientation dependence of geometrically necessary dislocations in polycrystalline aluminum during monotonic deformation: relationship to mechanical behavior. Mater. Sci. Eng.: A 2020:775.

[71] Doan D-Q, Tran A-S, Vu N-C. Grain and twin boundaries dependent mechanical behavior of FeCoCrNiCu high-entropy alloy. Mater. Today Commun. 2023;34.

[72] Huang CX, Wang YF, Ma XL, Yin S, Höppel HW, Göken M, Wu XL, Gao HJ, Zhu YT. Interface affected zone for optimal strength and ductility in heterogeneous laminate. Mater. Today 2018;21:713–9.

[73] Zhou Z, Li J, Wang Y, Mao Q, Liu Y, Yue Y, Huang C, Li Y. Effects of mechanical heterogeneity and dislocation storage capacity on the strength–ductility synergy of heterostructured laminates. Mater. Sci. Eng.: A 2024;896.

[74] Wang YF, Huang CX, He Q, Guo FJ, Wang MS, Song LY, Zhu YT. Heterostructure induced dispersive shear bands in heterostructured Cu. Scripta Materialia 2019; 170:76–80.

[75] Huang M, Xu C, Fan G, Maawad E, Gan W, Geng L, Lin F, Tang G, Wu H, Du Y, Li D, Miao K, Zhang T, Yang X, Xia Y, Cao G, Kang H, Wang T, Xiao T, Xie H. Role of layered structure in ductility improvement of layered Ti-Al metal composite. Acta Materialia 2018;153:235–49.

[76] Yuan F, Yan D, Sun J, Zhou L, Zhu Y, Wu X. Ductility by shear band delocalization in the nano-layer of gradient structure. Mater. Res. Lett. 2019;7:12–7.

[77] Jamalian M, Field DP. Effect of gradient microstructures on strengthening and toughening of AZ31. Mater. Sci. Eng.: A 2020;771.

[78] Hasan MN, Liu YF, An XH, Gu J, Song M, Cao Y, Li YS, Zhu YT, Liao XZ. Simultaneously enhancing strength and ductility of a high-entropy alloy via gradient hierarchical microstructures. Int. J. Plasticity 2019;123:178–95.

[79] Zhou Z, Wang Y, Li J, Mao Q, Liu Y, Yue Y, Li Y. Origins of HDI stress in copper–brass laminates with dual-heterostructured interfaces. Mater. Charact. 2024;210.

[80] Gao S, Yoshino K, Terada D, Kaneko Y, Tsuji N. Significant Bauschinger effect and back stress strengthening in an ultrafine grained pure aluminum fabricated by severe plastic deformation process. Scripta Materialia 2022;211.

[81] Mahato JK, De PS, Sarkar A, Kundu A, Chakraborti PC. Effect of deformation mode and grain size on Bauschinger behavior of annealed copper. Int. J. Fatigue 2016;83: 42–52.

[82] Zhang M, Bridier F, Villechaise P, Mendez J, McDowell DL. Simulation of slip band evolution in duplex Ti–6Al–4V. Acta Materialia 2010;58:1087–96.

[83] Charpagne MA, Hestroffer JM, Polonsky AT, Echlin MP, Texier D, Valle V, Beyerlein IJ, Pollock TM, Stinville JC. Slip localization in Inconel 718: A three-dimensional and statistical perspective. Acta Materialia 2021;215.

[84] Wang K, Sun Y, Yu H, Huang Y, Su S, Ning Z, Cheng Z, Fu W, Sun J, Liaw PK. Microstructure evolution and mechanical behavior of a CoCrFeNiMn0.75Cu0.25 high-entropy alloy by thermo-mechanical treatment. Mater. Sci. Eng.: A 2022;860.

[85] Marano A, Gélébart L, Forest S. Intragranular localization induced by softening crystal plasticity: analysis of slip and kink bands localization modes from high resolution FFT-simulations results. Acta Materialia 2019;175:262–75.

[86] Ahmadikia B, Kumar MA, Beyerlein IJ. Effect of neighboring grain orientation on strain localization in slip bands in HCP materials. Int. J. Plasticity 2021;144.

[87] B. Güler, Ü. Şimşek, T. Yalçinkaya, M. Efe, Grain-scale investigations of deformation heterogeneities in aluminum alloys, in, 2018.

[88] Dève H, Harren S, McCullough C, Asaro RJ. Micro and macroscopic aspects of shear band formation in internally nitrided single crystals of Fe-Ti-Mn alloys. Acta Metallurgica 1988;36:341–65.